Journal of
Materials Chemistry A

Accepted Manuscript

This article can be cited before page numbers have been issued, to do this please use: C. Wang, J. Wen, F. Luo, B. Quan, H. Li, Y. Wei, C. Gu and J. Li, *J. Mater. Chem. A*, 2019, DOI: 10.1039/C9TA00519F.

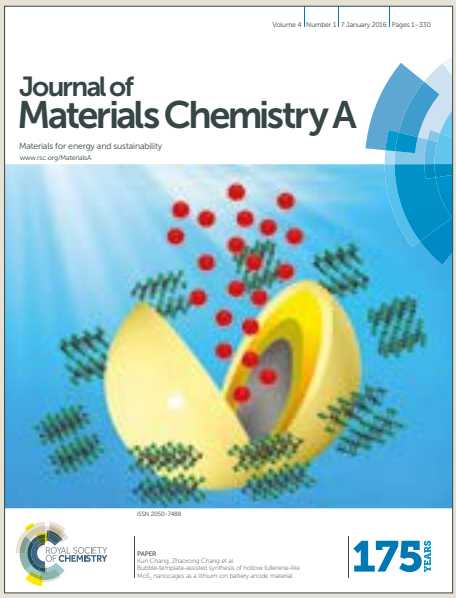

ROYAL SOCIETY OF CHEMISTRY

rsc.li/materials-a

View Article Online
DOI: 10.1039/C9TA00519F

Journal Name

ARTICLE

Anisotropic expansion and size-dependent fracture of silicon nanotubes during lithiation†

Received 00th January 20xx,
Accepted 00th January 20xx

DOI: 10.1039/x0xx00000x

www.rsc.org/

Chao Wang,‡[a,b] Jici Wen,‡[c,d] Fei Luo,[a] Baogang Quan,[a] Hong Li,[a,b] Yujie Wei,*[c,d] Changzhi Gu*[a,b] and Junjie Li*[a,b,e]

Silicon nanotube anodes are notably promising for high-performance lithium-ion batteries due to their outstanding structural stability, but fundamental understanding about their structural evolution during lithiation still remains unclear. Here, the expansion and fracture behavior of lithiated silicon nanotubes is investigated, and the influences of crystal phase, crystal orientation, inner radius, wall thickness, and thickness–radius ratio are demonstrated. Experiments and simulations demonstrate anisotropic expansion and outer-surface fractures of crystalline silicon nanotubes and isotropic expansion of amorphous ones. The inner holes of nanotubes undergo much less expansion than the outsides. The fracture ratio and the maximum hoop stress are positively correlated with both wall thickness and inner radius for crystalline silicon nanotubes. Their competition gives rise to an optimal thickness–outer radius ratio about 2/3, and the critical diameter reaches to 700 nm correspondingly. This research provides significant insight into the lithiation behavior of silicon nanotubes, which could help to design improved silicon anodes.

1. Introduction

Lithium-ion batteries have been commonly used in electric vehicles and portable electronics on account of their high energy density, high safety, and long cycle life.[1,2] Silicon is a highly promising anode material for next-generation lithium-ion batteries because of its high theoretical specific capacity of 4200 mAh g^{-1} (~10 times the capacity of conventional graphite) for forming $Li_{4.4}Si$.[3-5] However, tremendous volume expansion (~320%) occurs in silicon after full lithiation, which would result in structural pulverization of the active materials and further lead to rapid capacity fade.[6-8] Accordingly, various silicon nanostructures such as nanoparticles, nanowires, and nanotubes, have been applied to battery anodes to facilitate stress relaxation and avoid mechanical fractures.[9-14]

Although remarkable performance has been achieved by various nanostructured silicon anodes,[15,16] there is still plenty of room to tune those nanostructures for better resistance to failure and performance degradation during lithium insertion. Previous studies have shown the two-phase lithiation, isotropic deformation, and failure behavior of amorphous silicon nanoparticles; and a critical size up to 870 nm for amorphous silicon spheres has been reported.[17-19] Furthermore, anisotropic expansion and fracture of lithiated crystalline silicon nanowires and nanopillars have been shown and discussed, preferential expansion along <110> directions has been demonstrated, and a critical size of 300 nm for crystalline silicon nanowires has also been widely acknowledged.[20-23] These studies indicate that the structural change and degradation of silicon nanostructures have complex chemomechanical mechanisms related to crystal phase, crystal orientation, geometry shape, and structural size; thus different silicon nanostructures require different corresponding strategies to improve their electrochemical performance.[24-26]

Compared with other silicon nanostructures, silicon nanotubes are believed to better accommodate large volume change during lithiation due to the additional empty internal space.[27] Moreover, silicon nanotubes are also capable of promoting lithium ion diffusion because of the extra inner surfaces accessible to electrolyte and the shortened diffusion length for lithium ions.[28,29] However, for the lithiation behavior and structural evolution of silicon nanotubes, some fundamental understanding still remains unclear: How would crystal phase and crystal orientation influence the deformation and fracture behavior inside and outside the nanotubes? Is the capability to accommodate expansion in the internal space and the external space the same? Whether the inner hole and wall thickness have an optimal ratio for stress relaxation and fracture resistance? Answers to these questions could provide

[a] Beijing National Laboratory for Condensed Matter Physics, Institute of Physics, Chinese Academy of Sciences, Beijing 100190, P. R. China. *Email: jjli@iphy.ac.cn; czgu@iphy.ac.cn
[b] School of Physical Sciences, University of Chinese Academy of Sciences, Beijing 100049, P. R. China
[c] State Key Laboratory of Nonlinear Mechanics, Institute of Mechanics, Chinese Academy of Sciences, Beijing 100190, P. R. China. *Email: yujie_wei@lnm.imech.ac.cn
[d] School of Engineering Sciences, University of Chinese Academy of Sciences, Beijing 100049, P. R. China
[e] Songshan Lake Materials Laboratory, Dongguan, Guangdong, 523808, P. R. China
† Electronic Supplementary Information (ESI) available. See DOI: 10.1039/
‡ These authors contribute equally to this work.

View Article Online
DOI: 10.1039/C9TA00510F

a better understanding of the lithiation behavior and help to improve the cycling performance of silicon nanotube anodes. Thus, it is necessary to investigate the structural evolution such as shape change, volume change, and fracture behavior of silicon nanotubes during lithiation.

In this paper, we have fabricated well-designed silicon nanotube arrays by electron-beam lithography (EBL) and following Cr mask deposition and dry etching. The structural evolution of fully lithiated silicon nanotubes is studied, and the influences of crystal phase, crystal orientation (<100>, <110>, and <111>), inner radius, and wall thickness on the expansion and fracture behavior are also demonstrated. The optimal thickness–outer radius ratio and critical size to avoid fracture are discussed through comparison of the fracture ratios of <111> silicon nanotubes. Furthermore, finite element simulation on the stress-evolution in silicon nanotubes is carried out to better understand and interpret the lithiation behavior of silicon nanotubes. A robust electrochemical-mechanical coupling model is employed, and the simulation results are in good agreement with the experimental observations. Our work would enrich the fundamental research on various silicon nanostructures, inspire studies on silicon nanotubes, and help to design better silicon anodes for lithium-ion batteries.

2. Experimental section

2.1 Materials preparation

Silicon wafers (p-type, 500 ± 10 μm thick, 5-15 Ω · cm) with <100>, <110>, and <111> crystal orientations were directly used for crystalline silicon. Amorphous silicon was obtained by deposition on the silicon substrates using a Plasma Enhanced Chemical Vapor Deposition System (Plasmalab System 100, Oxford Instruments). SiH_4 (15 sccm) and Ar (475 sccm) were used as the precursor gas (1000 mTorr) with the temperature set at 120 °C and the HF power set at 10 W. The deposition time was 2 h to get a thick amorphous layer.

2.2 Silicon nanotube fabrication

The silicon substrates were first spin-coated by a 200-nm-thick PMMA (495 k) resist layer, exposed in an Electron-Beam Lithography System (Raith 150, Raith Company), and treated in 1 : 3 MIBK : IPA developer to form an annular patterned resist coating layer. A 50-nm-thick chromium layer was then deposited on the substrates by an Electron-Beam Evaporator System (FU-12PEB, F.S.E Corporation). After the lift-off process in acetone, the resist layer was moved out and only the annular Cr mask arrays stayed on the silicon substrates. Then the substrates were etched using the cryo-etching process with an Inductively Coupled Plasma Reactive Ion Etching System (PlasmaPro 100 Cobra, Oxford Instruments). SF_6 (45 sccm) and O_2 (8-10 sccm) were used as the etching gas (12 mTorr), and the etching time was 1 minute at 4 W of the RIE power and 700 W of the ICP power. The residual Cr mask was removed by dissolving in $(NH_4)_2Ce(NO_3)_6/CH_3COOH$ solution for one hour.

2.3 Electrochemical test

Swagelok-type batteries were made in an argon-filled glovebox with the as-fabricated silicon nanotubes as the working electrodes and lithium foils as the counter electrodes. Cu foil current collectors and polymer separators were used for the silicon nanotube electrodes. The electrolyte was 1 mol L^{-1} $LiPF_6$ in ethylene carbonate and dimethyl carbonate (EC/DMC, 1:1 by volume). Linear sweep voltammetry was carried out for lithiation of the batteries by a multichannel potentiostat system (VSP-300, Bio-Logic Science Instruments). The batteries were swept at 0.1 mV s^{-1} from the open circuit voltage to 10 mV vs. Li/Li^+, then held at 10 mV for 24 h to ensure complete lithiation of the silicon nanotubes.

2.4 Physical characterization

The batteries after electrochemical testing were disassembled in an argon-filled glovebox, where the lithiated silicon nanotube electrodes were washed with dimethyl carbonate to clean out the residual electrolyte and vacuum dried for hours afterwards. Then the samples were transferred to a scanning electron microscope (Helios 600i, FEI Company) for morphological and structural characterization. The samples were sealed in an argon-filled box when transferring from the glovebox to the sample chamber. The X-ray diffraction (XRD) measurements of silicon substrates were carried out by the conventional θ–2θ scan in a Bruker D8 ADVANCE system with the Cu *Kα* line.

3. Results and discussion

3.1 Fabrication of silicon nanotubes

The fabrication process of silicon nanotube arrays is illustrated in Fig. 1a. First, the silicon substrate coated with a PMMA layer is exposed in the EBL system and treated in the developer to get a patterned PMMA layer on the substrate. Second, a Cr layer is deposited on the patterned PMMA layer by electron-

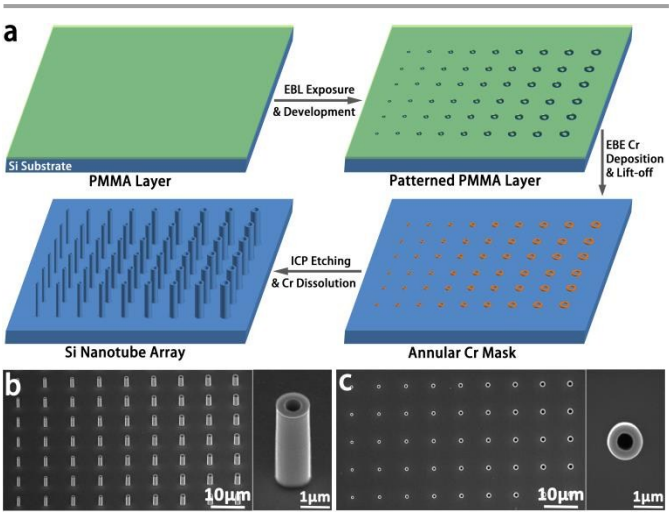

Fig. 1 Fabrication of silicon nanotubes. (a) Schematic illustration of fabrication process of silicon nanotube arrays. (b) Tilted angle and (c) top view SEM images of a typical silicon nanotube array and a single silicon nanotube. The silicon nanotube array is <111> orientated with wall thickness of 300 nm, height of 3.7 μm, and varying inner radius.

View Article Online
DOI: 10.1039/C9TA00519F

beam evaporator, and then only annular Cr mask arrays remain on the substrate after the lift-off process in acetone. Third, the silicon substrate with annular Cr mask arrays is etched by an inductively coupled plasma reactive ion etching (ICP) system. After removing the residual Cr mask, silicon nanotube arrays are obtained for further electrochemical lithiation.

For our research on structural evolution, the fabricated silicon nanotube arrays have several advantages as model anodes. First, the inner radius and wall thickness can be precisely controlled by modifying the corresponding exposure pattern. Second, the crystal directions in the cross section of the nanotubes can be easily identified by referring to the primary flat of the silicon wafer. Third, nanotube arrays are orderly arranged and vertically oriented with a uniform height, which is beneficial for both the morphological comparison and statistical analysis.

Four kinds of silicon substrates are used to fabricate <100>, <110>, <111>, and amorphous silicon nanotubes. The XRD spectra in Fig. S1 (ESI†) show the typical crystallographic properties of silicon substrates with <100>, <110>, and <111> crystal orientations. Five nanotube arrays with different wall thicknesses (100, 200, 300, 400, and 500 nm, respectively) are designed on each silicon substrate, as shown in Fig. S2a (ESI†). In each array, there are 100 rows of nanotubes, and the inner radii of nanotubes in each row are 100, 150, 200, 250, 300, 350, 400, 450, and 500 nm, respectively. Accordingly, the thickness–outer radius ratio (d/R) ranges from 1/6 to 5/6. The distance between two rows/columns is set to 8 μm to make sure that the expansion of silicon nanotubes does not affect each other.

Fig. 1b and c show the tilted angle and top view scanning electron microscope (SEM) images of a typical silicon nanotube array and a single silicon nanotube. The silicon nanotube array is <111> orientated with wall thickness of 300 nm, height of 3.7 μm, and varying inner radius from 100 nm to 500 nm. (high-magnification SEM images are shown in Fig. S2b). It can be seen in Fig. 1b and c that the silicon nanotubes are orderly aligned in the array and the nanotubes in each column of the array are of uniform size, which could make the observation and statistical analysis of the silicon nanotubes more convenient and convincing. Moreover, the silicon nanotube shows high verticality and sharp edge, which are attributed to the ICP etching.[30]

3.2 Lithiation of silicon nanotubes

To investigate the expansion and fracture behavior of the silicon nanotubes after full lithiation, the electrodes are linearly swept to 10 mV vs. Li/Li$^+$ at 0.1 mV s^{-1}, then held at 10 mV for 24 h to ensure complete lithiation. Fig. 2a–l show the SEM images of the <100>, <110>, <111>, and amorphous silicon nanotubes after lithiation in four columns, in which Fig. 2a–d show the low-magnification SEM images of the typical silicon nanotube arrays, Fig. 2e–h show the SEM images of silicon nanotubes with different expansion behavior but no fractures, and Fig. 2i–l show the SEM images of silicon nanotubes with the same original size but different fracture behavior. The SEM images of the pristine silicon nanotubes before lithiation are shown in Fig. S3 (ESI†), which are

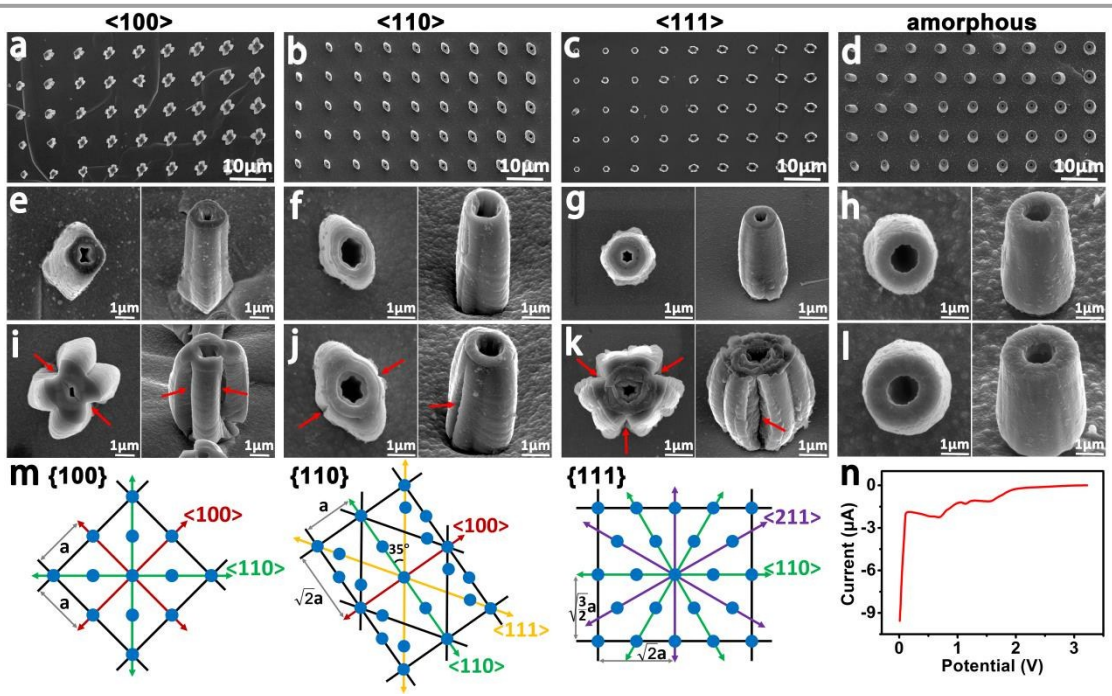

Fig. 2 Expansion and fracture behavior of silicon nanotubes after full lithiation. The SEM images are arranged in four columns for <100>, <110>, <111>, and amorphous silicon nanotubes, respectively. (a–d) Arrays of silicon nanotubes with different sizes. (e–h) Silicon nanotubes with different expansion behavior but no fractures. (i–l) Silicon nanotubes with different fracture behavior. The fractures are marked by the red arrows. (m) Schematics of the atomic distributions in {100}, {110}, and {111} crystal planes of silicon. (n) Typical current *vs* voltage curve during lithiation of the silicon nanotubes.

View Article Online
DOI: 10.1039/C9TA00510F

corresponding to the SEM images in Fig. 2 one by one. The wall thicknesses of the pristine silicon nanotubes are 300 nm (Fig. S3e–h) and 500 nm (Fig. S3i–l), while the inner radii of the pristine silicon nanotubes are 300 nm (Fig. S3g) and 500 nm (Fig. S3e, f, h–l). These images clearly show the anisotropic lateral expansion both inside and outside the crystalline silicon nanotubes. The outer surfaces of the initially annular cross-section of <100>, <110>, and <111> nanotubes change to cross, ellipse, and hexagon, respectively, which is consistent with the previous research of silicon nanopillars.[20] Interestingly, the insides of <100> nanotubes change to hollow cross with a rotation of 45°, while the insides of both <110> and <111> nanotubes change to hollow hexagon with certain rotation angles relative to the outsides.

Fractures are also observable in crystalline silicon nanotubes, as directed by the red arrows in Fig. 2i–k. The cracks occur at the outer surfaces of the nanotubes and propagate along the vertical axis, while the insides of the nanotubes are squeezed and distorted. The fracture locations of <100>, <110>, and <111> nanotubes are generally distributed at the four corners of the cross junction, the two ends of the minor axis of the ellipse, and the midpoints of the six sides of the hexagon, respectively. In addition, the middle part of the nanotube bulges out slightly relative to both ends, which can be associated with the attributes of strain that its relaxation is the largest away from sharp corners.[17,31]

The anisotropic expansion and fracture of crystalline silicon nanotubes could be explained by the preferential lateral expansion in <110> directions.[20,22,32] The interplanar spacing along <110> direction is larger than those along <100>, <111>, and <211> directions, providing a dominant ion channel for lithium implantation, thus leading to more significant expansion in <110> directions.[33] Fig. 2m shows the schematics of the atomic distributions of the <100>, <110>, and <111> nanotube cross-sections, i.e., the {100}, {110}, and {111} crystal planes. In {100} crystal plane, there are four mutually orthogonal <110> directions (green lines) bisected by four <100> directions (red lines), resulting in cross-shaped edge and a 45°-rotated hollow cross. In {110} crystal plane, there are two <110> directions (green lines), two <100> directions (red lines), and four <111> directions (yellow lines). The expansion in <111> directions is less than that in <110> directions but more than that in <100> directions due to the medium interplanar spacing,[34] thus leading to four small bumps around the minor axis of the ellipse; the hollow part is also shaped as hexagon because of the major expansion in <110> and <111> directions. In {111} crystal plane, there are six <110> directions (green lines) bisected by six <211> directions (purple lines), resulting in hexagon-shaped edge and a 30°-rotated hollow hexagon. The preferential lateral expansion in <110> directions could induce tensile stress concentration at the outer surfaces between <110> directions, especially at the angle bisector of <110> directions, and eventually lead to anisotropic fractures at these locations.[22] At the inner surfaces of the silicon nanotubes, the anisotropic inward expansion could induce compressive hoop stress, resulting in the squeezed and distorted hollow shapes. To verify our interpretation, the hoop stress distributions are further carried out in the following simulation part. In addition, the typical current *vs* voltage curve during initial lithiation is shown in Fig. 2n, which is consistent with the experiments of silicon nanopillars.[32]

For comparison, the expansion behavior of amorphous silicon nanotubes after full lithiation is also studied, as shown in Fig. 2d, h, and l. It can be seen that the lateral expansion is basically isotropic both inside and outside the silicon nanotubes, which is associated with the isotropic properties of amorphous silicon.[35] Interestingly, no fractures appear at all the fully lithiated amorphous silicon nanotubes in this study. Since the maximum outer diameter for the pristine nanotubes is 2 μm, it suggests that the critical diameter of the amorphous silicon nanotubes must be larger than 2 μm (in this paper, critical diameter for nanotubes refers to the critical outer diameter of the nanotubes). Compared to crystalline silicon nanotubes, amorphous silicon nanotubes show superior fracture resistance, which could be attributed to the homogeneous hoop stress during lithiation rather than stress concentration from anisotropic expansion,[18,36] as well as the stress relaxation due to the uniformly distributed flaw of rough amorphous silicon.[37]

Furthermore, the silicon nanotubes after initial lithiation and delithiation are also examined (Fig. S4, ESI †). For delithiation, the lithiated silicon nanotubes are linearly swept to 2 V vs. Li/Li^+ at 0.1 mV s^{-1}, then held at 2 V for 24 h. After delithiation, the silicon nanotubes contract back to smaller size compared to lithiated silicon nanotubes. The silicon nanotubes that avoid fracture during lithiation remain unfractured after delithiation, while the silicon nanotubes that fracture during lithiation get more severe cracks after delithiation due to the intense stress induced by lithium extraction. In addition, the silicon substrates also experience severe fractures due to the intense tensile stress during lithium extraction.

3.3 Statistical analysis on anisotropy

Statistical analysis on the expansion and fracture behavior of silicon nanotubes, which is shown in Fig. 3, is further accomplished to enrich the SEM observations. More than 50 silicon nanotubes are measured for each type of nanotubes. The error bars in the charts indicate the corresponding standard deviation. Fig. 3a shows the schematics of the cross-sectional shape of lithiated nanotubes and all the potential fracture locations (marked by red or purple arrows), where the fracture location is represented by the angle measured from the horizontal line to the fracture line. The variations of wall thickness, cross-sectional area and hollow area, height, and volume of silicon nanotubes after full lithiation are shown in Fig. 3b–e, respectively. The fracture locations at the outer surfaces of <100>, <110>, and <111> nanotubes are show in Fig. 3f–h, respectively. This systematical study on expansion and fracture behavior of silicon nanotubes would also enrich the fundamental research on hollow silicon nanostructures.

View Article Online
DOI: 10.1039/C9TA00519F

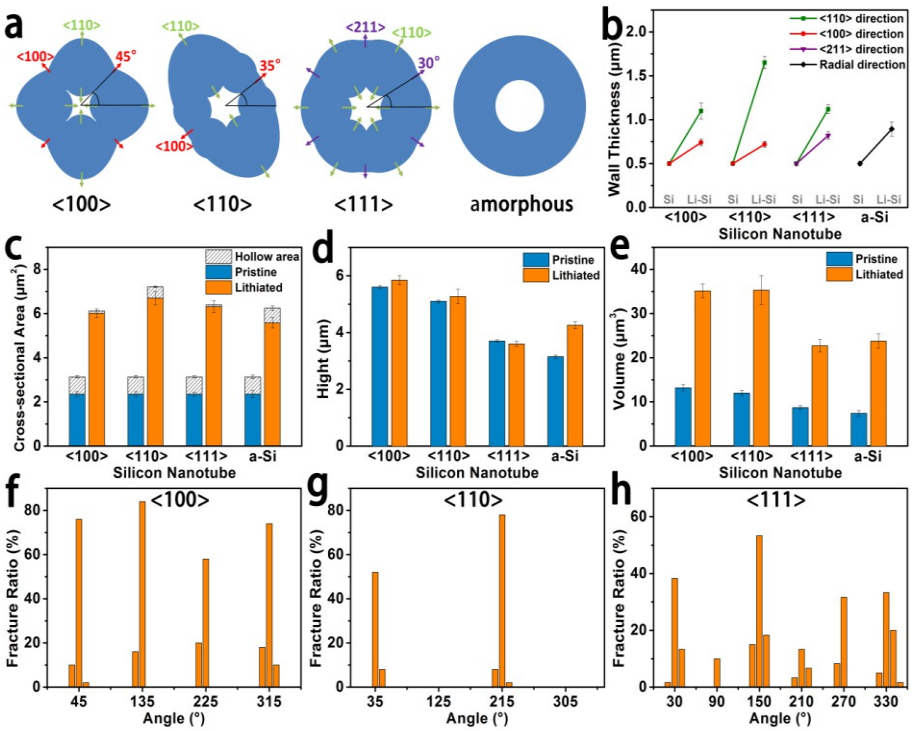

Fig. 3 Statistical analysis on the expansion and fracture behavior of the <100>, <110>, <111>, and amorphous silicon nanotubes after full lithiation. (a) Schematics of the cross-sectional shape and fracture angles of nanotubes. The variations of (b) wall thickness, (c) cross-sectional area and hollow area, (d) height, and (e) volume of silicon nanotubes. The fracture angle distributions of (f) <100>, (g) <110>, and (h) <111> silicon nanotubes.

Fig. 3b and c show that the variations of wall thickness and cross-sectional area are in good agreement with SEM observations. In the meanwhile, the expansion inward the inner hole is specially characterized by showing the changes of hollow area in Fig. 3c. It can be seen that the reduction in hollow area of <100> and <111> silicon nanotubes is more than that of <110> and amorphous silicon nanotubes, which is due to more severe extrusion with more preferentially expanded <110> directions in the cross section. Notably, the proportions of the reduction in hollow area to the increment in cross-sectional area are only 18.4%, 6.3%, 17.6%, and 3.6% for <100>, <110>, <111>, and amorphous silicon nanotubes, respectively. These low proportions indicate that the insides of the nanotubes undergo much less expansion than the outsides, thus the strain accommodation and stress relaxation are limited in the hollow area. The limited expansion in the hollow area might be associated with the deformation suppression by the compressive hoop stress and the compressive stress-induced slowing down of interfacial reaction and diffusion.[32,38,39]

Fig. 3d shows that the average height of <100>, <110>, <111>, and amorphous silicon nanotubes changes to 104%, 103%, 97%, and 135%, respectively. The height decrease of <111> silicon nanotubes after full lithiation is supposed to be associated with the collapse of {111} crystal planes.[20] It can be seen that the deformation in height is much less than the deformation in cross section; and this anisotropy is ascribed to the tubular free surfaces that can better accommodate the radial expansion than axial expansion.[40] Moreover, the height increase of amorphous silicon nanotubes is much greater than that of crystalline silicon nanotubes and closer to the radial increase of amorphous silicon nanotubes, which indicates that amorphous silicon tends to expand isotropically during lithiation even in an anisotropic structure. Fig. 3e shows that the average volume expansion of <100>, <110>, <111>, and amorphous silicon nanotubes after full lithiation reaches to 267%, 295%, 261%, and 321%, respectively, which is reasonable for lithiated silicon anodes considering the standard deviation.[41]

Fracture locations at the outer surfaces of the nanotubes are further studied. Fig. 3f shows that the fractures in <100> silicon nanotubes are concentrated around 45°, 135°, 225°, and 315°, which coincide with the four mutually orthogonal <100> directions on the cross section. Fig. 3g shows that the fractures in <110> silicon nanotubes are concentrated around 35° and 215°, coinciding with the two opposite <100> directions on the cross section. Fig. 3h shows that the fractures in <111> silicon nanotubes are concentrated around 30°, 90°, 150°, 210°, 270°, and 330°, which coincide with the six <211> directions on the cross section. These fractures bisect the angles formed by adjacent <110> directions, and are associated with the stress concentration from anisotropic expansion caused by preferential lithiation in <110> directions,[21,26] as previously illustrated in Fig. 2m. Especially, the fracture behavior related to the sizes of inner hole and outer shell of nanotubes is further studied in the following part.

View Article Online
DOI: 10.1039/C9TA00519F

3.4 Size-Dependent Fracture

Apart from crystal phase and crystal orientation, hollow size and wall thickness also have significant influences on the fracture behavior of silicon nanotubes. To further study this, the fracture ratios are counted for the <111> silicon nanotube arrays with varying sizes, as shown in Fig. 4. The tested electrode has 100 rows of nanotubes with varying wall thicknesses (100, 200, 300, 400, and 500 nm) and inner radii (100, 150, 200, 250, 300, 350, 400, 450, and 500 nm) in each row, and is swept to 10 mV vs. Li/Li$^+$ at 0.1 mV s^{-1} and held at 10 mV for more than 24 h. The different fracture behavior indicates the significant influences of wall thickness and inner radius on lithiated silicon nanotubes, and the orderliness and uniformity of the precisely fabricated silicon nanotube arrays contribute to clear and direct comparisons.

Fig. 4a shows the statistical data of the fracture ratios. It can be seen that the fracture ratios are highly correlated with the wall thickness and hollow size of the silicon nanotubes. When the wall thickness is 500 nm or the inner radius is larger than or equal to 400 nm, the fracture ratios of the silicon nanotubes reach to 100%. When the wall thickness is less than or equal to 200 nm and the inner radius is less than or equal to 150 nm, the fracture ratios of the silicon nanotubes drop to 0%. Within the size range of the study, the fracture ratio increases as the wall thickness or inner radius increases when other conditions remain unchanged. The positive correlation between fracture ratio and wall thickness can be explained by the size-dependent buildup of large tensile hoop stress in the surface layer, which is caused by the "pushing-out effect" of the lithiation-induced expansion at the two-phase interface.[24,42] The positive correlation between fracture ratio and inner radius is unexpected, implying that larger hollow area doesn't bring better stress relaxation and fracture resistance when the wall thickness is constant. Correspondingly, a competitive factor might be involved to facilitate fractures, which is supposed to be associated with the effect of the curvature of the nanotube wall on stress distribution, ion diffusion, and fracture resistance during anisotropic expansion.[43]

The correlations between fracture ratio and outer radius as well as wall thickness are further shown in Fig. 4b. When the outer radius is larger than or equal to 700 nm, the fracture ratios of the silicon nanotubes reach to 100%. When the outer radius is less than or equal to 250 nm, the fracture ratios of the silicon nanotubes drop to 0%. For the rest of outer radius values, the fracture ratio tends to decrease first and then increase as the wall thickness increases, and there is an optimal size of the nanotube for the lowest fracture ratio. The optimal thickness–outer radius ratios (d/R) are shown in Fig. 4c, which are determined by finding out the lowest fracture ratio of a specific outer radius from Fig. 4b, and the average d/R value is 0.68 (approximately 2/3) for outer radius from 300 nm to 650 nm. When the hollow size reaches to the optimal value ($r/\mathrm{R} = 1/3$, $d/\mathrm{R} = 2/3$), the increase of hollow size would bring higher fracture ratios. Under the condition of optimal d/R, the outer diameter corresponding to 0% fracture ratio could reach to 700 nm (outer radius of 350 nm), which is larger than the critical diameter (300 nm) of silicon

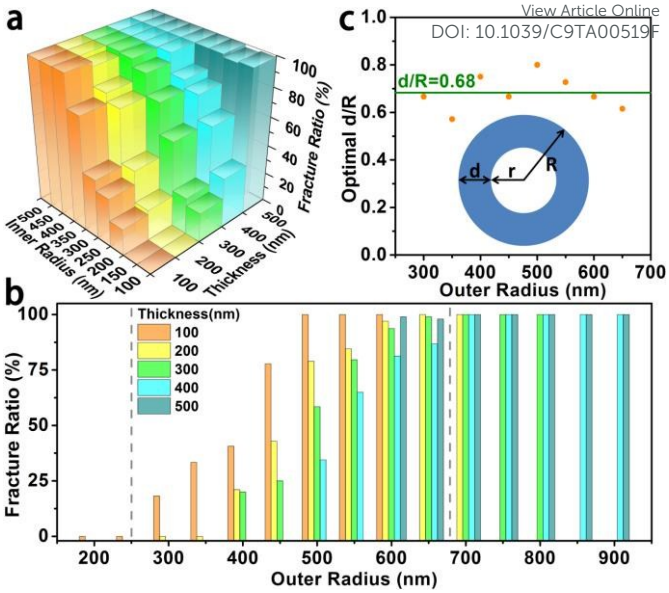

Fig. 4 Size-dependent fracture for <111> silicon nanotubes after full lithiation. Statistical data of the fracture ratios versus (a) inner radius and wall thickness, and (b) outer radius and wall thickness. (c) Optimal thickness–outer radius ratio (d/R) for the lowest fracture ratio of silicon nanotubes with different outer radii.

nanowires/nanopillars,[22,23] meaning silicon nanotubes have better fracture resistance than silicon nanowires/nanopillars. Moreover, the existence of optimal nanotube size implies the competition between wall thickness and inner radius that show complex effects on anisotropic fractures. A deeper understanding related to the stress evolution of the initial lithiation of silicon nanotubes is required.

3.5 Chemomechanical modeling

Accordingly, finite element simulation on the stress evolution in silicon nanotubes during initial lithiation is carried out to better understand the expansion and fracture behavior of silicon nanotubes. The electrochemical-mechanical coupling process for silicon nanotubes during lithiation is modeled in this part, of which the numerical procedure could be found in our previous work.[44,45]

According to Yang et al. and Zhang et al.,[24,26] the lithium ion diffusivity D is concentration dependent. We use the form of

$$D = D_0\,[1/(1-\bar{c}\,) - 2\alpha\bar{c}\,]$$

where D_0 is a diffusion constant, $\bar{c}$ is the normalized concentration, and α is a constant. We consider the diffusivity along different crystal orientations being anisotropic and assume $D_{0,<110>} = 6D_{0,<100>} = 60D_{0,<111>}$,[24] in which the diffusion coefficient $D_{0,<100>} = 2.0\times10^{-12}\ cm^2s^{-1}$.[46] A fully coupled constitute model are adopted, with the concentration-dependent elastic modulus E in the form:[47]

$$E = E_0 + m\bar{c}E_0$$

and the concentration-dependent yield strength captured by the voce model:[48]

$$\sigma_y = \sigma_{y0} + \bar{c}R_0\sigma_{y0} + R_\infty\sigma_{y0}(1-e^{-b\bar{c}})$$

View Article Online
DOI: 10.1039/C9TA00519F

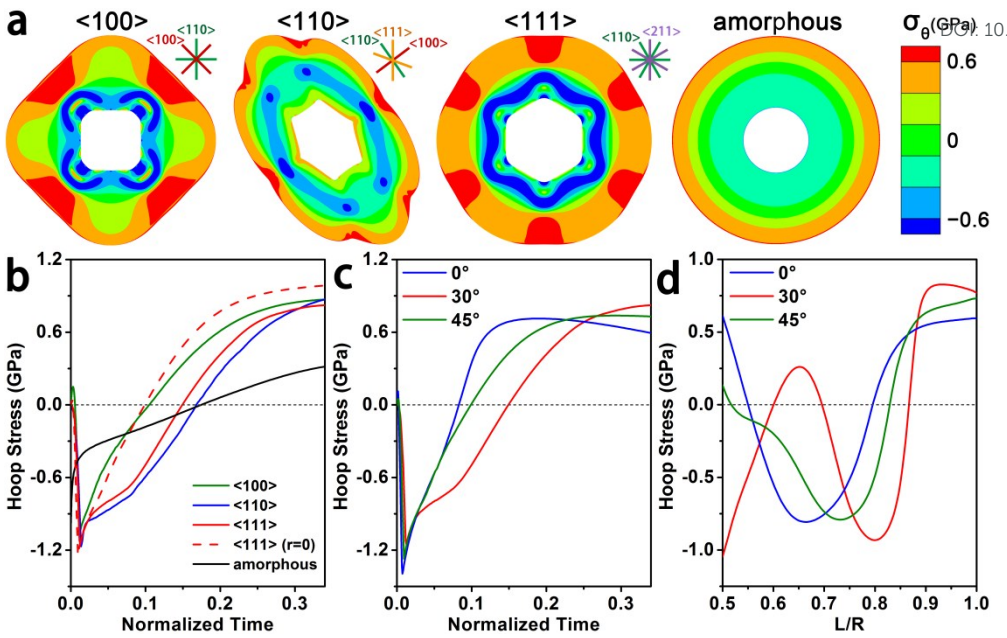

Fig. 5 Finite element simulation on the stress-evolution in lithiated silicon nanotubes with original sizes of $r = d = 100\ nm$. (a) Hoop stress contours of the cross-sections of <100>, <110>, <111>, and amorphous silicon nanotubes (left to right, in turn) at normalized lithiation time $t = 1/3$. (b) Hoop stress evolution at the potential fracture locations of <100>, <110>, <111>, and amorphous silicon nanotubes and <111> silicon nanopillars ($r = 0$ and $R = 200\ nm$) during lithiation. (c) Hoop stress evolution on the outer surface at 0°, 30°and 45°of <111> silicon nanotubes during lithiation. (d) Hoop stress distributions along the radii at 0°, 30°and 45° of <111> silicon nanotubes at normalized lithiation time $t = 1/3$. Here L ($r \le L \le R$) represents the radial coordinate in the original nanotube.

where $E_0 = 90.13\ GPa, m = -0.79, \sigma_{y0} = 9.0\ GPa, R_0 = -0.2, R_\infty = -0.75, b = 4$, and Poisson's radio $\upsilon = 0.22$.[45,49]

From left to right, we show in turn in Fig. 5a the hoop stress contours of the cross-sections of <100>, <110>, <111>, and amorphous silicon nanotubes at normalized lithiation time $t = 1/3$. It can be seen that the shapes of the cross-sections of the nanotubes are consistent with experimental observations. Tensile hoop stress concentration occurs at the outer surfaces of crystalline silicon nanotubes, while no stress concentration occurs in amorphous silicon nanotubes. More importantly, the locations of the maximum tensile hoop stress are in good agreement with the fracture locations observed in the experiments for crystalline silicon nanotubes, which verifies the interpretation that the tensile stress concentration determines the anisotropic fractures at the outer surfaces of nanotubes. As a contrast, the homogeneously distributed hoop stress enhances the fracture resistance of amorphous silicon nanotubes. In addition, the cumulated plastic strain contours of the cross-sections of nanotubes are shown in Fig. S5 (ESI†), where the locations of the plastic strain concentration are consistent with those of the hoop stress concentration.

Fig. 5b shows the hoop stress evolution at the potential fracture locations of <100>, <110>, <111>, and amorphous silicon nanotubes and <111> silicon nanopillars (i.e. nanotubes with $r = 0$) during lithiation. The silicon nanotubes and nanopillars have the same outer radius of 200 nm. With lithiation proceeding, the crystalline nanotubes show higher hoop stress than amorphous nanotubes and lower hoop stress than crystalline nanopillars, suggesting that silicon nanotubes have better fracture resistance than silicon nanopillars and that the amorphous silicon nanotubes have the best fracture resistance. Furthermore, Fig. 5c and d show the hoop stress evolution on the outer surface and the hoop stress distributions along the radii at 0°, 30°, and 45° of <111> silicon nanotubes, which are supplements to the hoop stress contours of the cross-sections in certain directions. It can be seen that the tensile hoop stress first appears in the <110> direction (0°), then reaches to a larger value in the <211> direction (30°), and eventually develops into tensile hoop stress concentration and fracture in <211> directions.

For the fabricated nanotube with inner radius r, wall thickness d, and outer radius R, two factors of the structure size need to be considered when considering fracture resistance. One is the average radius $\bar{r}$ as $\bar{r} = 1/2\ (r + R)$, and the other is the specific surface area B as $B = S/V = 2/d + 1/h$, where surface area $S = 2\pi h(r + R) + \pi(R^2 - r^2)$, volume $V = \pi h(R^2 - r^2)$, wall thickness $d = R - r$, and height h is constant for the nanotube arrays on the same substrate. We propose that $\bar{r}$ characterizes the effect of nanotube size on stress accumulation and distribution and that B characterizes the extent to which stress can be released.[40] Accordingly, we model the stress evolution of <111> silicon nanotubes with different sizes during initial lithiation.

Keep $d = 300\ nm$ with r changing from 100 nm to 500 nm, then B is a constant as well; hence the maximum hoop stress can only be influenced by the average radius $\bar{r}$ of the

View Article Online
DOI: 10.1039/C9TA00519F

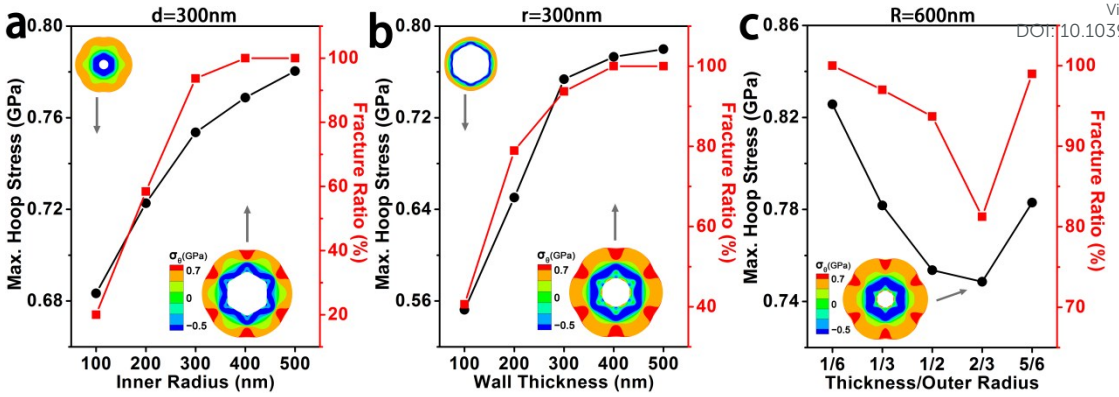

Fig. 6 Size-dependent hoop stress for lithiated <111> silicon nanotubes. The maximum hoop stress $\sigma_{\theta,max}$ (simulation results, black curve) and fracture ratio (experimental results, red curve) as functions of (a) inner radius r ($d = 300\ nm$), (b) wall thickness d ($r = 300\ nm$), and (c) thickness-outer radius ratio d/R ($R = 600\ nm$) for lithiated <111> silicon nanotubes. Insets: hoop stress contours of the nanotube cross-sections for (a) $r = 100\ nm$ and $400\ nm$, (b) $d = 100\ nm$ and $400\ nm$, and (c) $d/R = 2/3$ at normalized lithiation time $t = 1/3$.

nanotubes. It can be seen in Fig. 6a that $\sigma_{\theta,max}$, the maximum tensile hoop stress, increases as the inner radius r increases. This means that, as the average radius $\bar{r}$ of the nanotube structure increases, the structure has higher risk of fracture, which is in good agreement with experimental results as shown by the red curve in Fig. 6a. We also show the hoop stress contours of two representative nanotubes ($r = 100\ nm$ and $r = 400\ nm$) at normalized lithiation time $t = 1/3$ in the insets of Fig. 6a. It can be seen that the maximum hoop stress in tension locates at the outer surfaces of the <111> nanotubes along the <211> directions, and it is larger when $\bar{r}$ is larger, resulting in higher fracture ratio as observed in experiments.

We then examine the dependence of the maximum hoop stress $\sigma_{\theta,max}$ on the wall thickness d while keeping the inner radius r constant. For $r = 300\ nm$, we see from Fig. 6b that $\sigma_{\theta,max}$ increases as d increases. In the insets of Fig. 6b, we show the hoop stress contours of two representative nanotubes ($d = 100\ nm$ and $d = 400\ nm$) at normalized lithiation time $t = 1/3$. It can be seen that greater wall thickness gives rise to higher maximum stress, which is attributed to the increase of both $\bar{r}$ and B, thus leading to higher fracture ratio of the nanotubes, as shown by the red curve in Fig. 6b. The positive correlation between the maximum hoop stress and the inner radius or wall thickness in our simulation explains the positive correlation between the fracture ratio and the inner radius or wall thickness in the experiment.

Now we explore the influences of both wall thickness d and inner radius r when R is constant ($R = 600\ nm$). The maximum hoop stress as a function of d/R is shown in Fig. 6c. We can see that the maximum hoop stress decreases at first as d increases (r decreases), which is mainly caused by the decreasing of the average radius $\bar{r}$. As d continues to increase, the maximum hoop stress increases, because the specific surface area B decreases significantly and the diffusion induced volume change is constrained strongly. Combined with the influences of the average radius $\bar{r}$ and the specific surface area B, there is an optimal structure size for silicon nanotubes, which has the lowest maximum hoop stress and consequently the lowest fracture ratio (red curve in Fig. 6c) during lithiation. The transitional point where $\sigma_{\theta,max}$ minimizes at a specific $d/\mathrm{R} = 2/3$ is in good agreement with the experimental results, and the optimal $d_o/\mathrm{R} = 2/3$ is also instructive for designing silicon nanotube anodes with improved fracture resistance and electrochemical performance for lithium-ion batteries.

3.6 Discussion

Although lots of fundamental studies have been done on the lithiation of both crystalline and amorphous silicon, our work introduces another geometric factor, namely the inner hole, which constitutes the fundamental factor for nanostructure designing of silicon based anodes for lithium-ion batteries. Inner holes are considered as an effective way to alleviate lithiation-induced stress and enhance fracture resistance of silicon anodes, yet exactly in which way and to what extent the inner hole works are still questions worth exploring. To deeply understand the role of inner hole in silicon nanotubes, the sizes of inner hole and wall thickness have been systematically designed for SEM observation and statistical analysis. Finite element simulation has also been carried out to study the influences of inner hole on stress evolution. Experimental observations and simulation results are in good agreement. Our findings would bring the understanding of silicon nanotubes to a new level.

Apart from enriching the fundamental research on various silicon nanostructures and inspiring studies on silicon nanotubes, our results suggest several notable information, which can also answer the questions raised in the introduction part. First, crystal phase plays a significant role in fracture resistance despite of the existence of inner hole. Amorphous silicon nanotubes present excellent fracture resistance. Crystalline silicon nanotubes suffer anisotropic expansion at both insides and outsides, but fractures occur at the outer

View Article Online
DOI: 10.1039/C9TA00510F

surfaces due to tensile stress concentration. Second, the internal space of silicon nanotubes undergoes much less expansion than the external space. This suggests a deeper understanding on the role of inner hole: since the strain accommodation and the consequent stress relaxation are quite limited from the hollow space during lithiation, the enhancement of fracture resistance of silicon nanotubes is supposed to be mainly attributed to the reduction of stress accumulation caused by the replacement of lithiated silicon by hollow space. Third, the thickness–outer radius ratio has an optimal value for fracture resistance of crystalline silicon nanotubes. This suggests an unexpected fact that a larger inner hole does not always mean better enhancement of fracture resistance, and that the inner hole needs to be tuned to an appropriate ratio ($r/\mathrm{R} = 1/3$) for the best structural stability during lithiation. The absolute sizes of wall thickness, inner radius, and outer radius also need to be limited to the proposed critical values to alleviate fractures. These insightful perspectives are instructive for tuning silicon nanostructures to better resistance to failure and performance degradation during lithium insertion.

Notably, even though silicon nanotubes show limited inward expansion, they still have better fracture resistance than silicon nanopillars/nanowires on account that the critical diameter of crystalline silicon nanotubes (700 nm) is higher than that of crystalline silicon nanopillars/nanowires (300 nm). And the existence of optimal $d_o/\mathrm{R} = 2/3$ also means that the optimized hollow structure is better for the alleviation of structural damage than the solid structure of the same size. With the optimal structural design and the promoted lithium ion diffusion, silicon nanotubes would become excellent anode materials with enhanced electrochemical performance. In addition, it should be noted that this study mainly focuses on the initial cycle since the anisotropic expansion and the phase transition of silicon occur at this cycle. Due to the crack and pulverization of the supporting silicon substrates, subsequent cycles of silicon nanotubes cannot be studied by this model anode, which calls for a modified system in future studies.

Conclusions

In conclusion, we have fabricated well-designed silicon nanotube arrays and investigated the influences of crystal phase, crystal orientation, inner radius, and wall thickness on the expansion and fracture behavior of silicon nanotubes during initial lithiation. Experimental results are well explained by the finite element simulation based on a robust electrochemical-mechanical coupling model. Our research demonstrates isotropic lateral expansion without fractures in the amorphous silicon nanotubes even if the maximum original outer diameter is 2 μm; while anisotropic expansion and outer-surface fractures related to <110> directions occur in the crystalline silicon nanotubes. Particularly, the insides of nanotubes undergo much less expansion relative to the outsides. Statistical analysis and simulation results show that the maximum hoop stress and the fracture ratio of <111> silicon nanotubes are positively correlated with both wall thickness and inner radius in certain range. The optimal thickness–outer radius ratio d_o/R is approximately 2/3, under which the critical diameter to avoid fracture reaches to 700 nm for <111> silicon nanotubes. Our research provides significant insight into the structural evolution of silicon nanotubes during lithiation, which would enrich the fundamental research on various silicon nanostructures and help to design silicon nanotube anodes with improved electrochemical performance for lithium-ion batteries.

Conflicts of interest

There are no conflicts to declare.

Acknowledgements

This work is financially supported by the National Key R&D Program of China (Grant No. 2016YFA0200800, 2016YFA0200400, and 2016YFB0100500), the National Natural Science Foundation of China (Grant No. 91323304, 11674387, 11574369, 11574368，11574385，52315206, 51502334, and 11425211), the “Strategic Priority Research Program” of the Chinese Academy of Sciences (Grant No. XDB07020200, XDA09010000, and XDB22020200), and Key Research Program of Frontier Sciences of CAS (Grant No. QYZDJ-SSW-SLH042).

References

1 M. Armand and J.-M. Tarascon, *Nature*, 2008, **451**, 652-657.
2 K. Kang, Y. S. Meng, J. Bréger, C. P. Grey and G. Ceder, *Science*, 2006, **311**, 977-980.
3 X. Zuo, J. Zhu, P. Müller-Buschbaum and Y.-J. Cheng, *Nano Energy*, 2017, **31**, 113-143.
4 C. Wang, F. Luo, H. Lu, X. Rong, B. Liu, G. Chu, Y. Sun, B. Quan, J. Zheng, J. Li, C. Gu, X. Qiu, H. Li and L. Chen, *ACS Appl. Mater. Interfaces*, 2017, **9**, 2806-2814.
5 F. Luo, B. Liu, J. Zheng, G. Chu, K. Zhong, H. Li, X. Huang and L. Chen, *J. Electrochem. Soc.*, 2015, **162**, A2509-A2528.
6 N. Liu, H. Wu, M. T. McDowell, Y. Yao, C. Wang and Y. Cui, *Nano Lett.*, 2012, **12**, 3315-3321.
7 K. Feng, M. Li, W. Liu, A. G. Kashkooli, X. Xiao, M. Cai and Z. Chen, *Small*, 2018, **14**, 1702737.
8 S. Suresh, Z. P. Wu, S. F. Bartolucci, S. Basu, R. Mukherjee, T. Gupta, P. Hundekar, Y. Shi, T.-M. Lu and N. Koratkar, *ACS Nano*, 2017, **11**, 5051-5061.
9 X. Zhou, Y. X. Yin, L. J. Wan and Y. G. Guo, *Adv. Energy Mater.*, 2012, **2**, 1086-1090.
10 S. Chen, L. Shen, P. A. van Aken, J. Maier and Y. Yu, *Adv. Mater.*, 2017, **29**, 1605650.
11 C. K. Chan, H. Peng, G. Liu, K. McIlwrath, X. F. Zhang, R. A. Huggins and Y. Cui, *Nat. Nanotechnol.*, 2008, **3**, 31-35.
12 V. Chakrapani, F. Rusli, M. A. Filler and P. A. Kohl, *J. Power Sources*, 2012, **205**, 433-438.
13 M.-H. Park, M. G. Kim, J. Joo, K. Kim, J. Kim, S. Ahn, Y. Cui and J. Cho, *Nano Lett.*, 2009, **9**, 3844-3847.
14 J. K. Yoo, J. Kim, Y. S. Jung and K. Kang, *Adv. Mater.*, 2012, **24**, 5452-5456.
15 X. Su, Q. Wu, J. Li, X. Xiao, A. Lott, W. Lu, B. W. Sheldon and J. Wu, *Adv. Energy Mater.*, 2014, **4**, 1300882.
16 C. Wang, F. Luo, H. Lu, B. Liu, G. Chu, B. Quan, J. Li, C. Gu, H. Li and L. Chen, *Nanoscale*, 2017, **9**, 17241-17247.

17 Y. He, X. Yu, G. Li, R. Wang, H. Li, Y. Wang, H. Gao and X. Huang, *J. Power Sources*, 2012, **216**, 131-138.
18 J. W. Wang, Y. He, F. Fan, X. H. Liu, S. Xia, Y. Liu, C. T. Harris, H. Li, J. Y. Huang and S. X. Mao, *Nano Lett.*, 2013, **13**, 709-715.
19 M. T. McDowell, S. W. Lee, J. T. Harris, B. A. Korgel, C. Wang, W. D. Nix and Y. Cui, *Nano Lett.*, 2013, **13**, 758-764.
20 S. W. Lee, M. T. McDowell, J. W. Choi and Y. Cui, *Nano Lett.*, 2011, **11**, 3034-3039.
21 X. H. Liu, H. Zheng, L. Zhong, S. Huang, K. Karki, L. Q. Zhang, Y. Liu, A. Kushima, W. T. Liang and J. W. Wang, *Nano Lett.*, 2011, **11**, 3312-3318.
22 S. W. Lee, M. T. McDowell, L. A. Berla, W. D. Nix and Y. Cui, *Proc. Natl. Acad. Sci. U. S. A.*, 2012, **109**, 4080-4085.
23 J. W. Choi, Y. Cui and W. D. Nix, *J. Mech. Phys. Solids*, 2011, **59**, 1717-1730.
24 H. Yang, S. Huang, X. Huang, F. Fan, W. Liang, X. H. Liu, L.-Q. Chen, J. Y. Huang, J. Li and T. Zhu, *Nano Lett.*, 2012, **12**, 1953-1958.
25 S. C. Jung, J. W. Choi and Y.-K. Han, *Nano Lett.*, 2012, **12**, 5342-5347.
26 H. Yang, F. Fan, W. Liang, X. Guo, T. Zhu and S. Zhang, *J. Mech. Phys. Solids*, 2014, **70**, 349-361.
27 H. Wu, G. Chan, J. W. Choi, I. Ryu, Y. Yao, M. T. McDowell, S. W. Lee, A. Jackson, Y. Yang, L. Hu and Y. Cui, *Nat. Nanotechnol.*, 2012, **7**, 310-315.
28 Y. Son, S. Sim, H. Ma, M. Choi, Y. Son, N. Park, J. Cho and M. Park, *Adv. Mater.*, 2018, **30**, 1705430.
29 M. Ge, J. Rong, X. Fang and C. Zhou, *Nano Lett.*, 2012, **12**, 2318-2323.
30 S. Tian, X. Xia, W. Sun, W. Li, J. Li and C. Gu, *Nanotechnology*, 2011, **22**, 395301.
31 J. L. Goldman, B. R. Long, A. A. Gewirth and R. G. Nuzzo, *Adv. Funct. Mater.*, 2011, **21**, 2412-2422.
32 G. Sandu, L. Brassart, J.-F. Gohy, T. Pardoen, S. Melinte and A. Vlad, *ACS Nano*, 2014, **8**, 9427-9436.
33 X. H. Liu, J. W. Wang, S. Huang, F. Fan, X. Huang, Y. Liu, S. Krylyuk, J. Yoo, S. A. Dayeh and A. V. Davydov, *Nat. Nanotechnol.*, 2012, **7**, 749-756.
34 C. Xiao, J. Guo, P. Zhang, C. Chen, L. Chen and L. Qian, *Sci. Rep.*, 2017, **7**, 40750.
35 N. Fukata, T. Subramani, W. Jevasuwan, M. Dutta and Y. Bando, *Small*, 2017, **13**, 1701713.
36 L. A. Berla, S. W. Lee, I. Ryu, Y. Cui and W. D. Nix, *J. Power Sources*, 2014, **258**, 253-259.
37 Y. Xu, E. Swaans, S. Chen, S. Basak, P. P. R. Harks, B. Peng, H. W. Zandbergen, D. M. Borsa and F. M. Mulder, *Nano Energy*, 2017, **38**, 477-485.
38 B. Ding, H. Wu, Z. Xu, X. Li and H. Gao, *Nano Energy*, 2017, **38**, 486-493.
39 X. H. Liu, F. Fan, H. Yang, S. Zhang, J. Y. Huang and T. Zhu, *ACS Nano*, 2013, **7**, 1495-1503.
40 T. Song, J. Xia, J.-H. Lee, D. H. Lee, M.-S. Kwon, J.-M. Choi, J. Wu, S. K. Doo, H. Chang and W. I. Park, *Nano Lett.*, 2010, **10**, 1710-1716.
41 Y. Yao, M. T. McDowell, I. Ryu, H. Wu, N. Liu, L. Hu, W. D. Nix and Y. Cui, *Nano Lett.*, 2011, **11**, 2949-2954.
42 X. H. Liu, L. Zhong, S. Huang, S. X. Mao, T. Zhu and J. Y. Huang, *ACS Nano*, 2012, **6**, 1522-1531.
43 J.-L. Zang and Y.-P. Zhao, *Int. J. Eng. Sci.*, 2012, **61**, 156-170.
44 J. Wen, Y. Wei and Y.-T. Cheng, *J. Power Sources*, 2018, **387**, 126-134.
45 J. Wen, Y. Wei and Y.-T. Cheng, *J. Mech. Phys. Solids*, 2018, **116**, 403-415.
46 J. Pan, Q. Zhang, J. Li, M. J. Beck, X. Xiao and Y.-T. Cheng, *Nano Energy*, 2015, **13**, 192-199.
47 V. B. Shenoy, P. Johari and Y. Qi, *J. Power Sources*, 2010, **195**, 6825-6830.
48 E. Voce, *Metallurgia*, 1955, **51**, 219-226.
49 F. Fan, S. Huang, H. Yang, M. Raju, D. Datta, V. B. Shenoy, A. C. Van Duin, S. Zhang and T. Zhu, *Modell. Simul. Mater. Sci. Eng.*, 2013, **21**, 074002.

Table of Contents Entry

View Article Online
DOI: 10.1039/C9TA00519F

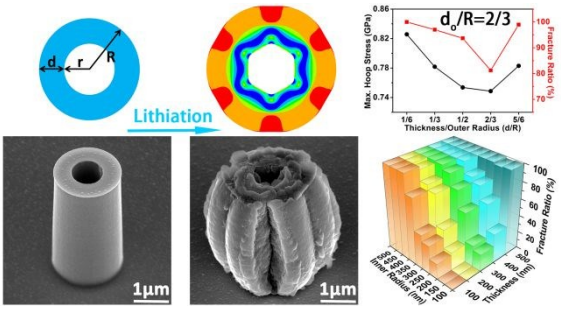

Experiments and simulations demonstrate anisotropic expansion and size-dependent fracture of silicon nanotubes during initial lithiation by well-designed nanotube arrays